Available online at www.sciencedirect.com

jmr&t Journal of Materials Research and Technology

journal homepage: www.elsevier.com/locate/jmrt

Original Article

Microstructure and thermal-physical properties of hypereutectic Al-Ni alloys

Liling Mo [a], *Xiong Zhou* [a], *Xuhong Liu* [a], *Meiyan Zhan* [a], *Yu-Jun Zhao* [b,*], *Jun Du* [a,**]

[a] School of Materials Science and Engineering, South China University of Technology, Guangzhou, 510640, China
[b] Department of Physics, South China University of Technology, Guangzhou, 510640, China

ARTICLE INFO

Article history:
Received 10 March 2023
Accepted 19 April 2023
Available online 27 April 2023

Keywords:
Al–Ni alloy
Microstructure evolution
Thermal-physical property
First-principles calculation

ABSTRACT

The microstructure and thermal-physical properties of Al-xNi (x = 6–25 wt.%) alloys were investigated by experiments first. With the increase of Ni content, the volume fraction and size of the Al_3Ni increase significantly, while the morphology has no change. The thermal expansion coefficient (CTE) and the thermal conductivity (TC) decrease at the same time. The CTE of Al-6 wt.%Ni alloy is 20.2×10^{-6}/K at 100 °C, decreasing to 15.4×10^{-6}/K for Al-25 wt.%Ni, which demonstrates favorable thermal expansion performance. The TC changes from 202.8 W/(m·K) to 103.9 W/(m·K). Besides, the structure and thermal properties of Al_3Ni were studied by the first-principles calculation to provide relevant thermodynamic data. The expansion performance was analyzed at the same time, the linear CTE of Al_3Ni is 13.82×10^{-6}/K at 100 °C. Based on the experiments and first-principles calculations, the modified Turner and general Effective Medium Theory (GEMT) models were used to explain the relationships between microstructure and thermal expansion coefficient, thermal conductivity of Al-xNi alloys.

1. Introduction

With the rapid development of 5G communications, integrated circuits and new energy vehicles, many devices place higher demands on thermal conductivity (TC), electrical conductivity (EC) and thermal expansion properties [1–5]. For example, improving the TC of the frame and shell materials enables faster heat release in mobile phones. In addition to higher TC, a low thermal expansion coefficient (CTE) makes some motor components such as pistons less susceptible to tightening and jamming at operating temperatures. Therefore, improving the TC, EC and CTE is crucial for the development of electronic devices. Aluminum (Al) is believed to have potential application in the field of heat dissipation for its high EC and TC [1]. However, the poor mechanical properties and high CTE of pure Al limit its wide application.

* Corresponding author. Department of Physics, South China University of Technology, 381 Wushan Rd, Guangzhou, 510640, Guangdong, China.
** Corresponding author. Department of Metallic Materials, School of Materials Science and Engineering, South China University of Technology, 381 Wushan Rd, Guangzhou, 510640, Guangdong, China.
E-mail addresses: zhaoyj@scut.edu.cn (Y.-J. Zhao), tandujun@sina.com (J. Du).
https://doi.org/10.1016/j.jmrt.2023.04.168

Alloying is an effective method to improve the properties of Al alloys. Nickel (Ni) is one of the common elements in Al for its low solubility and the formation of Al_3Ni phase. Al–Ni alloy has a high eutectic temperature (about 640 °C), considerable casting ability, thermal tear resistance and mechanical properties. Recently, it was found to have the prospect of replacing the commonly used Al–Si alloys [6].

In the past few decades, many studies have been carried out on the microstructure revolution and high temperature mechanical properties of Al–Ni alloys. Deng et al. prepared high-strength and heat-resistant Al-5.7 wt.% Ni alloy by selective laser melting, the tensile strength of the alloy at room temperature and 300 °C were 410 MPa and 140 MPa [7]. Kakitani studied the microstructure characteristics of Al-6.3 wt.% Ni alloy obtained by directional solidification at different cooling rates, the relationship between spacing of eutectic colonies and tensile properties was analyzed [8]. Fan et al. studied the morphological and crystallographic characteristics of Al–Al_3Ni eutectic structure, and found that the excellent thermal stability of Al–Al_3Ni eutectic can be attributed to the existence of the eutectic layer [9]. Peng et al. prepared Al-10 at.% Ni alloy by directional solidification, it was found that good strength and ductility can be obtained for the finer Al_3Ni phase was the dominant phase at a higher growth rate [10]. Adding trace alloying elements to improve the properties of Al–Ni alloys has also received extensive attention, Sc, Zr and Yb have been proven to have good modification effects [6,11,12]. In addition, to reduce the CTE of the Al–Ni alloy, it is necessary to increase the content of Ni to form a large volume fraction of the compounds. Nevertheless, research on the effect of Ni content on the microstructure, EC, TC and CTE has not been systematically studied to our knowledge, especially for the hypereutectic Al–Ni alloys.

Due to the low solid solubility of Ni in Al ($\leq$ 0.05 wt.%), the exceeded adding Ni will precipitate in the form of Al_3Ni. The elongated primary or fibrous-like eutectic Al_3Ni will hinder the transmission of free electrons in the heat conduction process, thus reducing the TC of the alloy. The linear CTE of Al_3Ni is smaller than that of pure Al according to our calculation results. Therefore, the addition of Ni in Al alloy often yields the reduction of CTE and TC with an increased volume fraction of Al_3Ni phase. Modeling the CTE and TC of alloys is of interest to many heat transfer applications. The rule of mixture (ROM), Turner, Kerner and Schapery models have been developed for the theoretical prediction of CTE [4,13–16]. The simulation of CTE models in Al-based composites has been performed and was well consistent with the experiment results [4,17]. However, the CTE of Al alloys simulated by CTE models has rarely been reported yet. The commonly used theoretical models of TC include the Solute atom model [18,19], Parallel model [20], Series model [20,21], Maxwell model [22,23] and the Effective Medium Theory (EMT) model [20,24]. These models are associated with the phase composition and microstructure, such as phase property, size, morphology and distribution, and have made some progress in high TC Mg alloys and binary Al alloys [19,20]. Despite this, the applicability of TC models in Al alloys needs further verification owing to the multiple factors. Besides, the intrinsic properties of phases are important for the analysis and construction of theoretical models, but they are difficult to obtain through experiments. The first-principles calculation method has been widely accepted to analyze the structural stability, mechanical, thermodynamic and thermos-physical properties of secondary phases [25–33].

Understanding the effects of Ni on the microstructure and thermal-physical properties is the basis for developing industrial applications of Al alloys in electronic devices. In this paper, the effects of Ni content on the microstructure, CTE, EC and TC of binary Al–Ni alloys were analyzed. The properties of Al_3Ni were studied by the first-principles calculations. Based on the experiments and first-principles calculation results, the effects of Ni on the microstructure, CTE and TC were quantified, which provided a theoretical basis for the development of Al alloys with excellent thermal-physical properties.

2. Methodology

2.1. Experiments

The hypereutectic Al-xNi alloys (x = 6, 10, 15, 20, 25 wt.%, mass percent, the same below) were designed by using industrial pure aluminum (Al $\geq$ 99.8) and pure nickel (Ni $\geq$ 99.99). The raw materials were added to the clay graphite crucible and put into the resistance furnace, then heated to the temperature of 50~80 °C above the melting points of Al-xNi alloys. After the slag of the melt was skimmed, the melt was poured into a steel mold with a size of 15 mm × 95 mm × 30 mm.

The obtained ingots were cut, ground and polished. The samples were etched with 0.5% HF, then the microstructures of the Al–Ni alloys were observed by optical microscope (OM, Leica DMI 3000, Leica, Germany) and scanning electron microscope (SEM, Zeiss Gemini 300, Carl Zeiss, Germany). The chemical compositions of different phases were quantitatively determined by energy dispersive spectroscopy (EDS, Oxford X-MaxN, Oxford, UK). The constituent phases of the samples were identified by X-ray diffraction (XRD, X'pert Powder, PANalytical). The sample was prepared with a size of 15 mm × 4 mm × 4 mm, then the CTEs were measured by a thermal dilatometer (TMA Q400) and the samples were heated from 25 °C to 200 °C at a rate of 5 °C/min. The thermal diffusivity (α) was obtained by the flash method (Netzsch LFA457) at 25 °C [34], and the size of the sample was Φ12.7 mm × 3 mm. The density (ρ) of the sample was determined by precision density balance (XHB-3000Z II) using Archimedes drainage method. Constant pressure heat capacity was calculated by the Neumann-Kopp rule. Five and three samples were tested for TC and CTE to minimize the experimental uncertainties. Then the thermal conductivity can be calculated by Eq. (1) [35]:

$$\lambda = \alpha \cdot \rho \cdot C_p \tag{1}$$

where α, ρ and Cp represent the thermal diffusivity, density and constant pressure heat capacity of the alloy, respectively.

2.2. Computational details

The theoretical calculation was carried out using the Vienna *ab-initio* simulation package (VASP) based on the density functional theory (DFT) [36]. The generalized gradient approximation (GGA) was used to calculate the exchange-

correlation energy of electrons. For this purpose, the Perdew-Burke-Ernzerhor (PBE) function was selected [37]. The standard frozen nuclear potential was used to describe the interaction between ions and electrons. The electron–ion interaction was characterized by the 3*s*, 3*p* valence states of Al atom, the 3*d*, 4*s* valence states of Ni atom. According to the convergence tests, the cutoff energy was set to 400 eV. The 15 × 15 × 8 K-point grid was used to generate an irreducible Brillouin zone in orthogonal Al_3Ni compound following the Monkhorst–Pack scheme. The structure was completely relaxed for the energy convergence to 10^{-6} eV. The minimum Hellman-Feynman force of each atom was chosen to be less than −0.01 eV/Å. Density functional perturbation theory (DFPT) and quasi-harmonic approximation (QHA) were used to study the phonon and thermodynamic properties of the optimized structure, respectively [38,39]. For this purpose, a 2 × 2 × 1 supercell was used to estimate the force constants, which was performed by the Phonopy program package [40].

3. Results

3.1. Experimental results

3.1.1. Microstructures of Al-xNi alloys

The optical microstructures, SEM images and the corresponding EDS results of Al-xNi alloys are shown in Figs. 1 and 2. The near eutectic Al–6Ni alloy is composed of α-Al and the eutectic structure, as shown in Fig. 1 (a). With the increase of Ni content, the strip-like Ni-rich primary phase arranged in different directions is precipitated, the size and amount of primary Ni-rich phase boost with the increase of Ni content. Fig. 2 is the SEM images and the corresponding EDS results. There is mainly consists of fibrous (α-Al + Al_3Ni) structure in Al–6Ni alloy. With the increase of Ni content, more primary Al_3Ni phase is precipitated. However, the morphology of primary Al_3Ni has not changed with the increase of Ni content. The XRD patterns of the Al-xNi alloys are shown in Fig. 3. Cubic α-Al and orthorhombic Al_3Ni phases were detected in the as-cast Al-xNi alloys, in line with the EDS results.

3.1.2. Thermal expansion coefficients, thermal/electrical conductivities of Al-xNi alloys

Fig. 4 shows the variation of CTEs of Al-xNi alloys with temperature and Ni content. With the increase of Ni content, the CTEs of Al-xNi alloys show a downward trend. In addition, the CTEs of Al–Ni alloys increase rapidly at first and then gently with the temperature increase. The CTE is 20.2 × 10^{-6}/K for Al–6Ni at 100 °C, with the Ni content increasing to 25 wt.%, the CTE decreases to 15.4 × 10^{-6}/K at 100 °C. The decrease of the CTEs is mainly due to the increase of volume fraction of Al_3Ni phase, which has a lower CTE than Al.

The heat capacity, density, thermal diffusivity, EC and TC of Al-xNi alloys are shown in Fig. 5. Due to the low specific heat of Ni element (for 0.46 J/(g·K)), the heat capacities of Al-xNi alloys decrease with the addition of Ni. The densities of the Al-xNi alloys increase with the increase of Ni content, while the thermal diffusivities decrease linearly. The TC of each alloy was calculated by the obtained thermal diffusivity, heat capacity and density. The ECs of Al-xNi alloys were also measured, the results are shown in Fig. 5(c). It can be seen that the EC and TC of Al-xNi alloys decrease linearly with the increase of Ni content. The EC decreases from 30.2 MS/m to 17.0 MS/m, and the TC decreases from 202.8 W/(m·K) to 103.9 W/(m·K).

3.2. The first-principles calculation

3.2.1. Structural properties

To study the thermal conductivity and thermal expansion mechanism of Al-xNi alloys further, the properties of Al_3Ni were analyzed by first-principles calculations. For a given system, the negative formation enthalpy means that the structure is thermodynamic stable. The formation enthalpies of 2~5 times cell structures in Al–Ni system were calculated to determine the most stable configuration. Besides, the common Al–Ni intermetallic compounds like Al_9Ni_2, Al_3Ni_2,

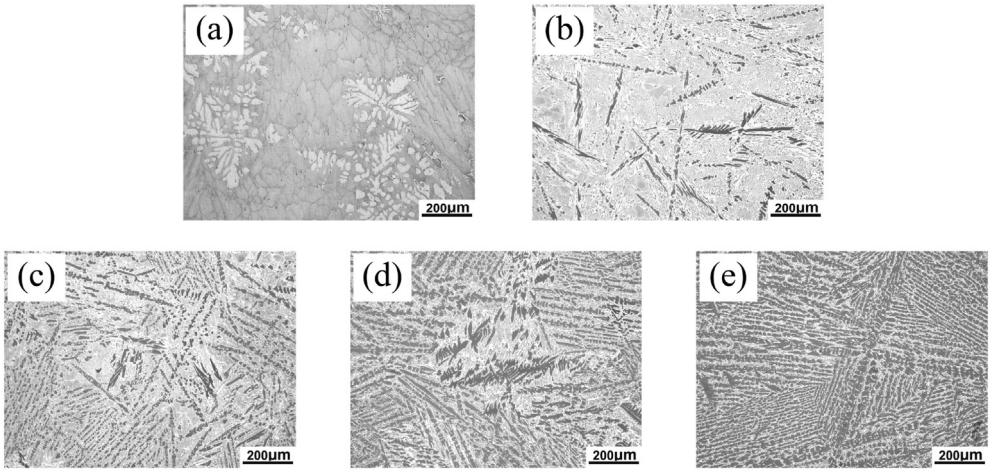

Fig. 1 – Optical images of Al-xNi alloys (x = 6~25 wt.%): (a) Al-6Ni, (b) Al-10Ni, (c) Al-15Ni, (d) Al-20Ni, (e) Al-25Ni.

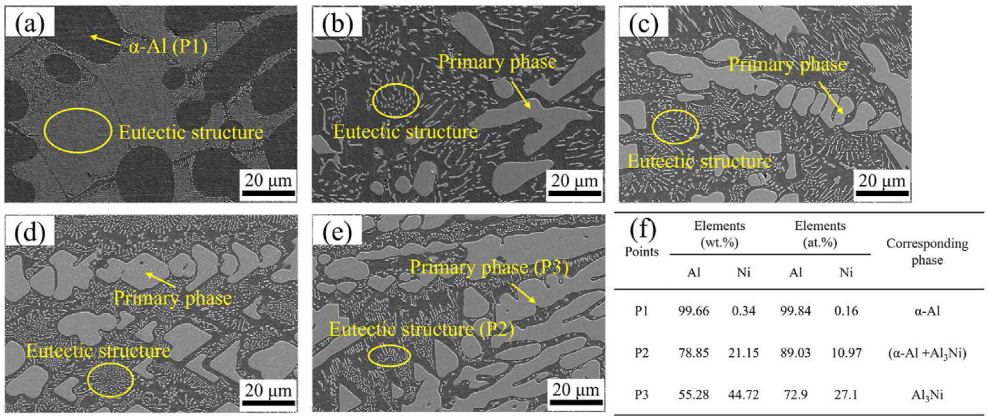

(f)

Points	Elements (wt.%) Al	Ni	Elements (at.%) Al	Ni	Corresponding phase
P1	99.66	0.34	99.84	0.16	α-Al
P2	78.85	21.15	89.03	10.97	(α-Al +Al_3Ni)
P3	55.28	44.72	72.9	27.1	Al_3Ni

Fig. 2 – SEM images of Al-*x*Ni alloys (*x* = 6~25 wt.%): (a) Al-6Ni, (b) Al-10Ni, (c) Al-15Ni, (d) Al-20Ni, (e) Al-25Ni, (f) the corresponding EDS results.

Al_4Ni_3, AlNi, Al_2Ni_3, Al_3Ni_5, $AlNi_2$, $AlNi_3$, Al_4Ni_{15} were considered. The formation enthalpies were calculated by:

$$\Delta H = \frac{H_{Al_xNi_y} - xH_{Al} - yH_{Ni}}{(x+y)} \quad (2)$$

among them, $H_{Al_xNi_y}$, H_{Al}, H_{Ni} represent the total energies of the Al–Ni compounds, Al and Ni elements, *x* and *y* represent the number of Al or Ni atom in the compounds, respectively.

The formation enthalpies of Al–Ni structures under the different composition ratios are shown in Fig. 6, the black line indicate the stable structure with the lowest formation enthalpy. It is obvious that most of the configurations have negative formation enthalpy at 0 K. According to the calculation results, Al_9Ni_2 and Al_3Ni tend to form for their negative formation enthalpies at the low Ni concentration case. However, the Al_9Ni_2 is slightly deviated from the black line in the convex point graph, as shown in Fig. 6, and phase separation may occur. Besides, Al_9Ni_2 is a metastable phase according to reference [41]. In an Al-rich Al–Ni alloy, the precipitation sequence is as follows: supersaturated solid solution → metastable phase, Al_9Ni_2 → stable phase, Al_3Ni [41]. Therefore, only the stable precipitate Al_3Ni existed in the actual solidification process in Al-rich Al–Ni alloy and was studied in the present work. The crystal structure of Al_3Ni is shown in Fig. 7. Besides, the detailed crystal information is listed in Table 1. The calculated results in this study are in good agreement with the literature [42].

3.2.2. *Thermal properties of Al_3Ni*

Thermal-physical properties are mainly related to their vibration energy and are shown by the associated thermodynamic parameters. The finite displacement calculation was carried out after the Al_3Ni crystal was scaled to different volumes first. Then the energy–volume curve was fitted by the Bird–Murnaghan equation of state, and the thermodynamic parameters related to the temperature such as bulk modulus, Grüneisen parameter, heat capacity and thermal expansion coefficient were also calculated. The total energy as a function of the corresponding volume is shown in Fig. 8(a). The most stable volume of Al_3Ni is 235.5 $Å^3$ at 0 K and ambient pressure.

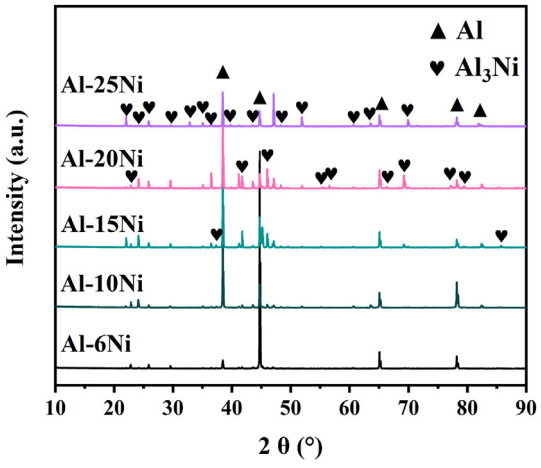

Fig. 3 – XRD patterns of Al-*x*Ni alloys (*x* = 6~25 wt.%).

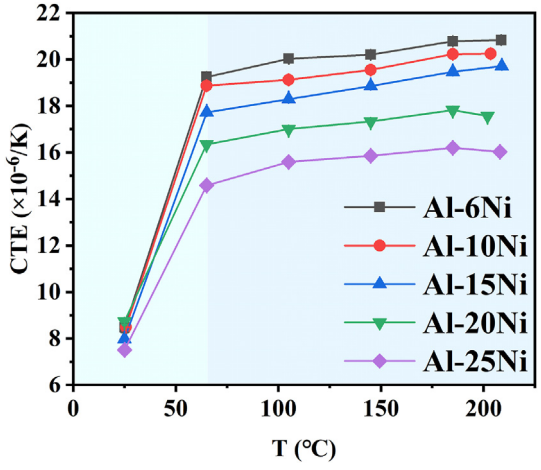

Fig. 4 – The thermal expansion coefficient (CTE) curves of Al-*x*Ni alloys (*x* = 6~25 wt.%) at 25–200 °C.

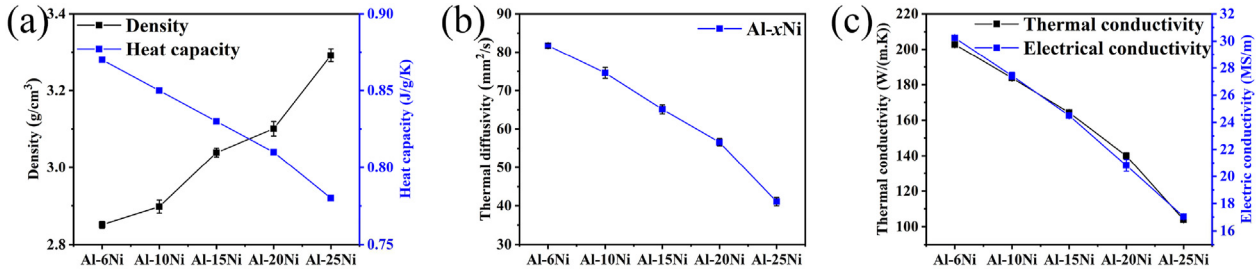

Fig. 5 – (a) Heat capacity and density, (b) thermal diffusivity, (c) electrical and thermal conductivity of Al-*x*Ni alloys (*x* = 6~25 wt.%).

The Birch-Murnaghan state equation was fitted, Fig. 8(b) is the Helmholtz free energy varies with cell volume and temperature of Al_3Ni, with the black line connecting the equilibrium volume, temperature and energy. As the temperature increases from 0 to 1000 K, the equilibrium volume increases and corresponding free energy decreases at different temperatures. The increment of the equilibrium volume is caused by the lattice vibration and thermal expansion.

The thermodynamic parameters vary with the temperature of Al_3Ni are shown in Fig. 9, including bulk modulus (B_V), heat capacity (C_p), Grüneisen parameters and linear thermal expansion coefficient. The variation of bulk modulus with temperature is shown in Fig. 9(a), which shows a downward tendency. As shown in Fig. 9(b), the heat capacity of Al_3Ni is increasing with the temperature. The Grüneisen parameter changes with temperature is shown in Fig. 9(c). It can be seen that the Grüneisen parameter is positive at 0~1000 K, meaning that the Al_3Ni shows thermal expansion characteristics. The linear CTE of Al_3Ni increases sharply first and then slowly with the increase of temperature, indicating that the volume of Al_3Ni expands with the change of temperature, which is consistent with the results of Figs. 8 and 9(c).

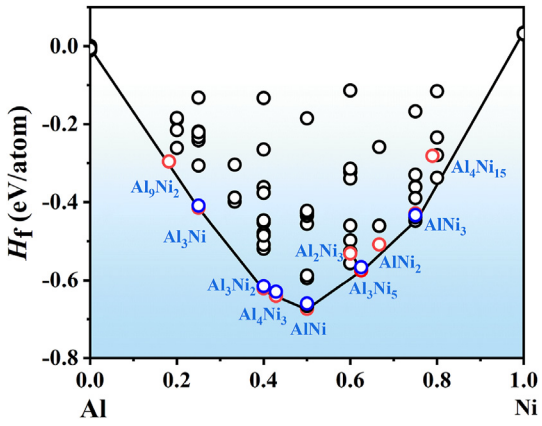

Fig. 6 – Formation enthalpies of Al–Ni alloys with consideration of 2, 3, 4, and 5-times primitive cell, the black line indicate the stable structure with the lowest formation enthalpy, the red and blue circles are the common Al–Ni compound as well as the results from Aflow [43].

3.2.3. *Electronic property*

The electronic property of Al_3Ni was studied from the aspects of band and density of states (DOS), with the results shown in Fig. 10. It can be observed from Fig. 10(a) that the valence and conduction bands overlap at the Fermi level in the high symmetry direction, which means that the Al_3Ni possesses the metal property. According to the peak intensity of the DOS and PDOS, most of the intensity is contributed by the *d* electron of Ni, and influence the strength of chemical bond between Ni–Ni atoms.

4. Discussion

4.1. *Relationship between microstructure and thermal expansion coefficient*

The thermal expansion coefficient of the alloy is mainly related to the intrinsic properties, content and distribution of the precipitated phase. With the Ni content increases from 6 wt.% to 25 wt.%, the Al atom is consumed and formed Al_3Ni with lower CTE, the volume fraction of Al_3Ni phase increased significantly at the same time, resulting in the decline of the CTE. The CTE curve of Al–Ni alloy with the same composition shows two stages, as shown in Fig. 4. The first stage is a linear increase stage, the CTE of the alloy increases linearly and

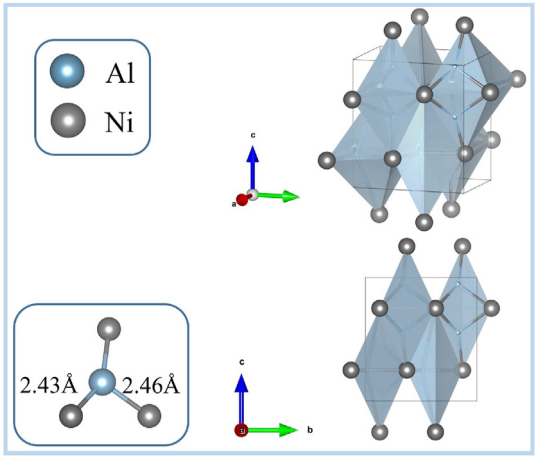

Fig. 7 – The crystal structure of Al_3Ni.

Table 1 – The crystal structure parameters and formation enthalpies of Al_3Ni.

Phase	Space group	Lattice parameters	V_{cell} (Å^3)	Formation enthalpies ΔH (eV/atom)	
				This work	Reference
Al_3Ni	Pnma	$a = 4.81$ Å, $b = 6.56$ Å, $c = 7.29$ Å $\alpha = \beta = \gamma = 90°$	229.90	−0.41	−0.405 [42]

rapidly at 25~100 °C. The small vibration amplitude of the atom, faint stress between the matrix and the precipitated phase may be the main reasons. As the temperature rises to above 100 °C, the vibration amplitude of the atoms increases and the lattice undergoes anharmonic vibration. However, the modulus of Al_3Ni is higher than Al matrix, and the expansion tendency is smaller, as shown in Figs. 9–11. At this time, massive Al_3Ni phase formed and interact with the Al matrix. The Al_3Ni with low CTE has a certain inhibitory effect on the thermal expansion of the α-Al, resulting in a small decrease in the CTE of the alloy. The high volume fraction Al_3Ni phase with low CTE can obstruct the Al matrix to make the CTE curves slow down.

Using the theoretical model to predict CTE is an effective way to estimate the CTE of a two-phase composite. The most commonly used CTE models were briefly discussed in reference [4]. According to previous studies [4,17,44], the Turner model is suitable for describing the relationship between microstructure evolution and thermal expansion properties in hypereutectic aluminum alloys. The Turner model assumes that the deformation of each component is equal to the overall deformation of every composite while ignoring the inside shear force. The expression is as follow [16]:

$$\alpha_c = \frac{\alpha_p V_p B_p + \alpha_m V_m B_m}{V_p B_p + V_m B_m} \tag{3}$$

among them, α_p, V_p, B_p are the thermal expansion coefficient, volume fraction, bulk modulus of the intermetallic compounds, α_m, V_m, B_m represent the thermal expansion coefficient, volume fraction, bulk modulus of the matrix, α_c is the predicted total thermal expansion coefficient of the alloy. The linear CTE (α_p and α_m), bulk modulus (B_p and B_m) of Al_3Ni and α-Al at 0~200 °C were obtained by the theoretical calculation, as shown in Fig. 11(b)–(c).

The volume fractions (V_m and V_p) of the α-Al, Al_3Ni were counted by the Image Pro Plus software, as shown in Fig. 11(a).

The results at 50, 100, 150 and 200 °C obtained by the conventional Turner model are shown in Fig. 12. The predicted values by the traditional Turner model are higher than the experimental values. Since the data of the phase used in the model are calculated by applying continuous deformation from −5% to +5% to the perfect crystal and heating up from 0 to 1000 K, the fitting curve is a continuous line with the same trend. In addition, the Turner model is proposed based on the composite material, and it is considered that the strain change in the heating deformation process is uniform. However, the size of the second phase in this study is large and can be divided into fibrous eutectic structure and lath primary phase. There are significant differences in morphology, size and deformation behavior between the primary and the eutectic phases, and it seems inappropriate to regard them as the same material in the modeling process. In order to describe the relationship between the microstructure and properties in hypereutectic alloys better, the composite modulus (Bc) was used to consider the Al_3Ni in the eutectic structure and primary phase separately, which was calculated by [4]:

$$B_c = \frac{\frac{V_p B_p}{3B_p+4G_m} + \frac{V_m B_m}{3B_m+4G_m}}{\frac{V_p}{3B_p+4G_m} + \frac{V_m}{3B_m+4G_m}} \tag{4}$$

here, G_m is the shear modulus of the matrix, the G of Al is 30.21 GPa in this work.

The value of Bc for (α-Al + Al_3Ni) eutectic structure and the fitting results using the modified Turner model are shown in Fig. 13. It can be seen that the predicted results by the modified Turner model are consistent with the experiments.

4.2. *Relationship between microstructure and thermal conductivity*

The microstructure of the Al–6Ni alloy is mainly the (α-Al + Al_3Ni) eutectic structure, and the free electrons have a

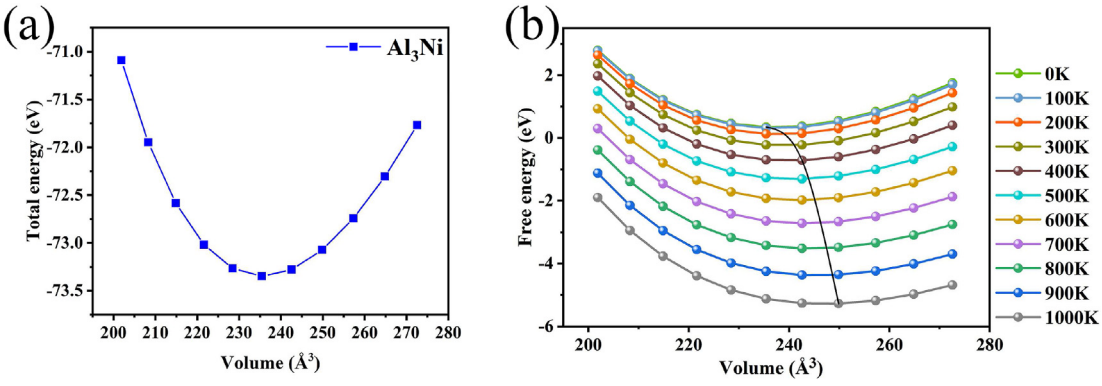

Fig. 8 – (a) Total energy changes with the cell volume of Al_3Ni at 0 K and 0 GPa, (b) free energies of Al_3Ni vary with cell volume and temperatures. The black line in (b) links the equilibrium volumes at different temperatures.

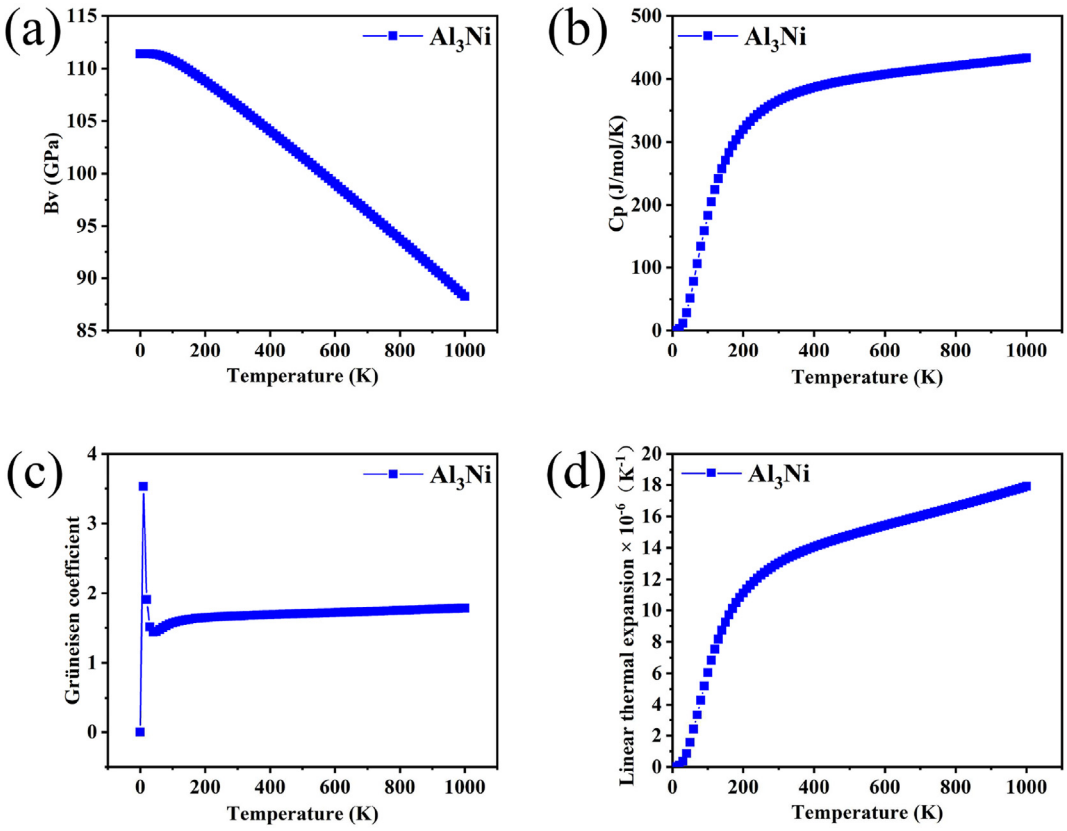

Fig. 9 – The change of B_v, C_p, Grüneisen coefficient and linear expansion coefficient with temperature of Al_3Ni.

large number of transfer channels during the transport process. With the increasing Ni content, the primary Al_3Ni precipitated and formed coarse blocks, as shown in Figs. 1 and 2, which impeded the free electron motion process. At the same time, the volume fraction of Al_3Ni increased significantly, from 10.1% to 49.8%, as shown in Fig. 11(a). Therefore, with the composition increasing to 25 wt.%, the volume fraction and size of Al_3Ni phase increase sharply, the interface between the primary phase and the matrix increases. Then the scattering effect of free electrons increases, which reduces the average free path of free electrons and deteriorates the thermal conductivity of the alloy as a result. Besides, the tendency of TC and EC of the Al-xNi alloys are almost the same, which proves that free electron is the main dominator for the heat transfer process.

In order to further understand the mechanism of thermal conductivity, the relationship between microstructure evolution and thermal conductivity of Al-xNi alloys was analyzed by the thermal conductivity model. The hypereutectic Al-xNi alloys are considered to be a two-phase system composed of matrix and Al_3Ni. In addition, the Al_3Ni and α-Al can be regarded as randomly distributed in the alloy, which meets

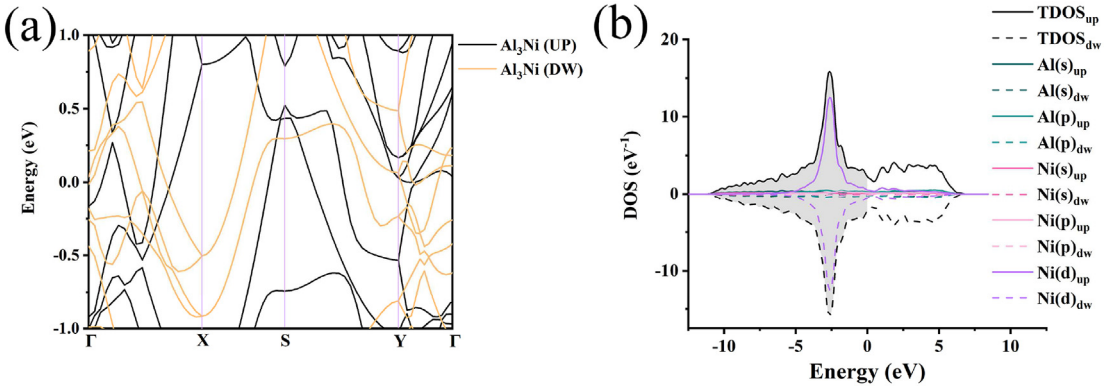

Fig. 10 – The band structures and density of states of Al_3Ni.

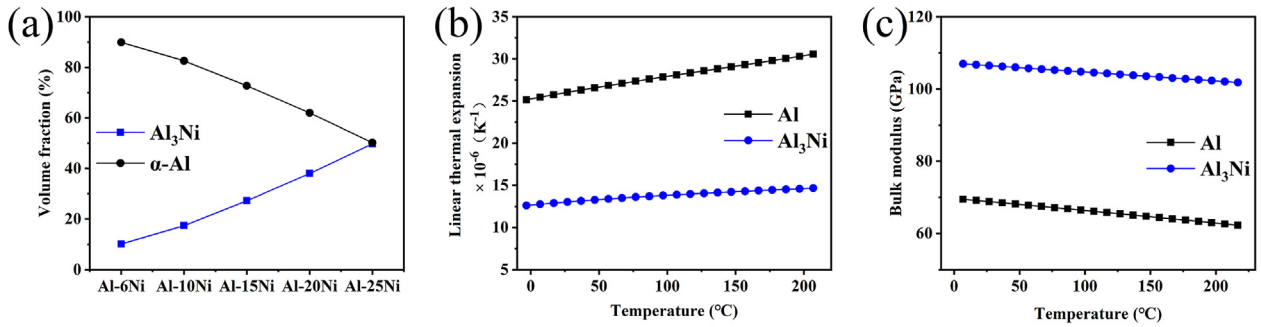

Fig. 11 – (a) The volume fraction of α-Al, Al_3Ni phases in Al-*x*Ni alloys (*x* = 6~25 wt.%), (b)–(c) the linear expansion coefficients and bulk modulus of α-Al and Al_3Ni at 0~200 °C.

the microstructure characterized by the Effective Medium Theory (EMT) model. However, the EMT model cannot reflect the actual shape and distribution of the second phase in the Al alloys, especially for the hypereutectic alloys. Therefore, a general Effective Medium Theory (GEMT) was proposed [45,46]:

$$\lambda = \frac{\sum_{i=1}^{m} \lambda_i V_i \frac{d_i k_0}{(d_i-1)k_0+\lambda_i}}{\sum_{i=1}^{m} V_i \frac{d_i k_0}{(d_i-1)k_0+\lambda_i}} \quad (5)$$

where λ_i is the thermal conductivity of phase, V_i is the corresponding volume fraction, m is the component fraction, d_i represents the different heat conduction mode, k_0 is the shape factor parameter.

According to the literature [47], $d_i = 3$. The TC of the Al matrix was considered to be $\lambda_m = 258$ W/(m·K) to simplify the calculation. For the TC of the Al_3Ni phase, Stadler believed that the value is 20~35 W/(m·K) [3]. In this study, the TC of Al_3Ni phase was chosen to be 32 W/(m·K). The volume fractions of the α-Al and Al_3Ni were counted by the Image Pro Plus software, as shown in Fig. 11(a). In addition, the Euler distance was used to optimize the value of the shape factor, which can be used to express the discrepancy between the two matrices. The smaller the Euler distance, the more

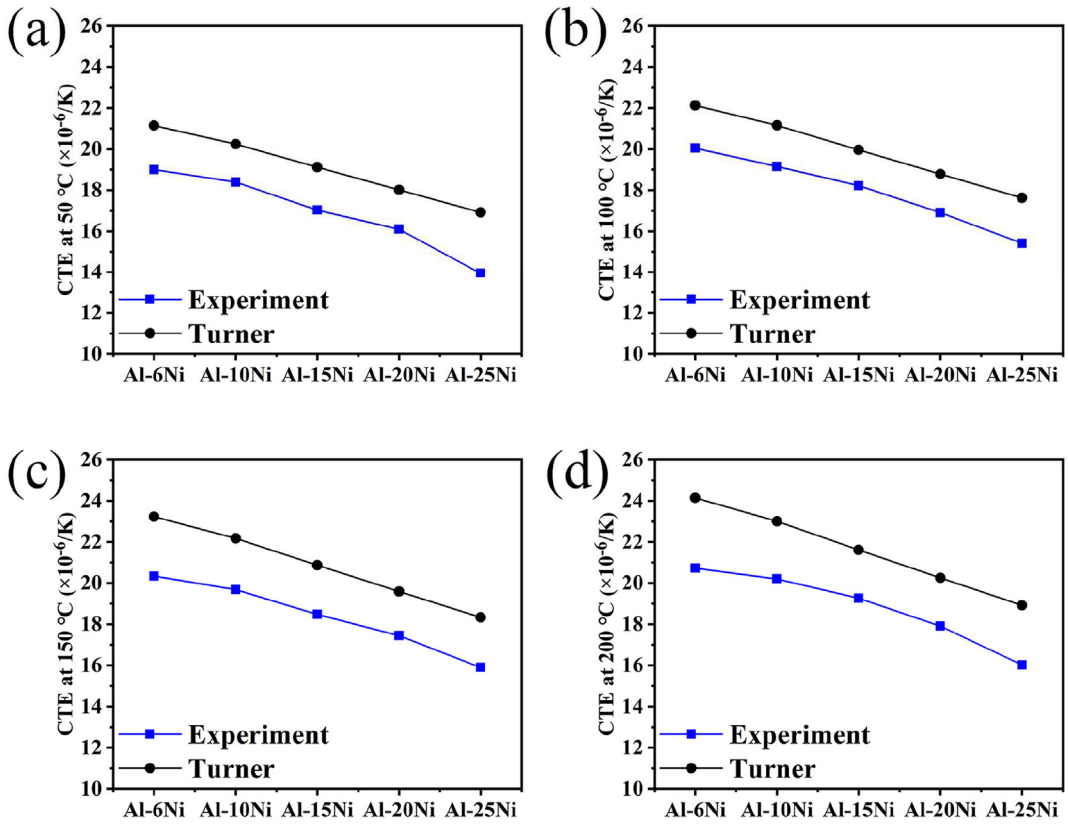

Fig. 12 – Turner model fitting results of thermal expansion properties for Al-*x*Ni alloys (*x* = 6~25 wt.%) at 50 °C, 100 °C, 150 °C, 200 °C.

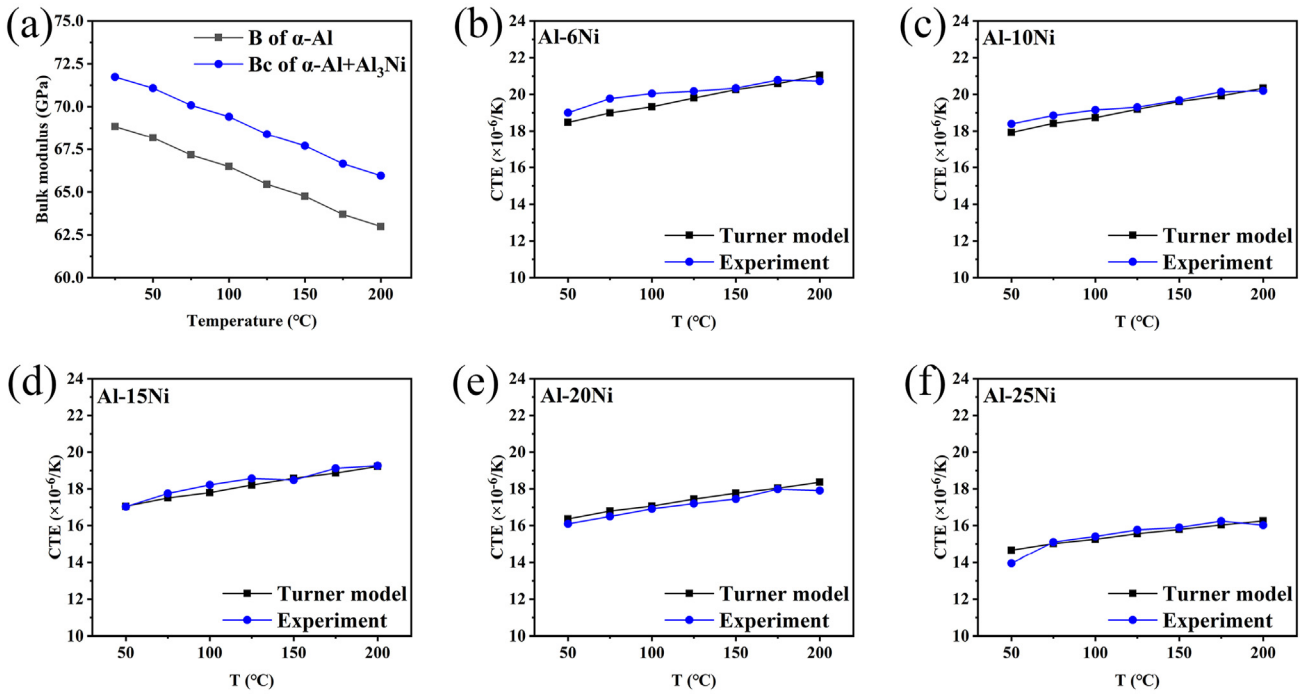

Fig. 13 – (a) Turner model and (b)–(e) the revised Turner model fitting results of thermal expansion properties for Al-xNi alloys (x = 6~25 wt.%).

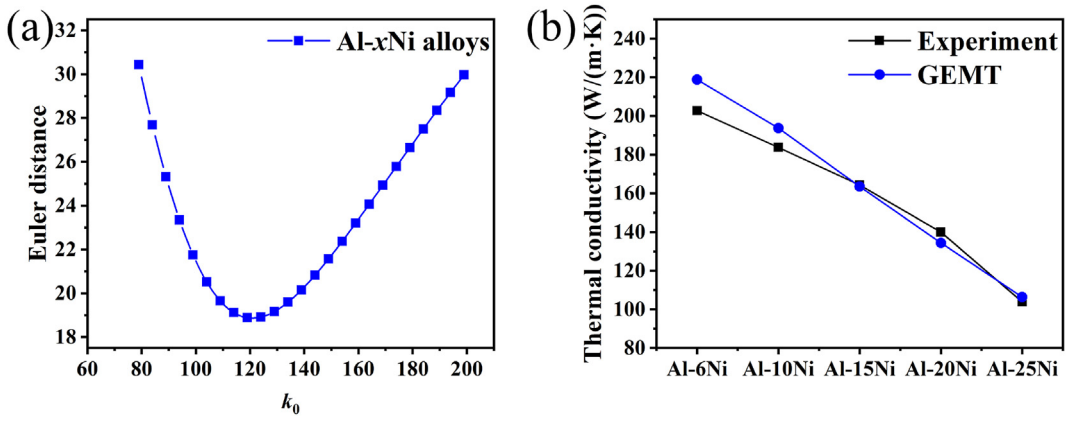

Fig. 14 – (a) The Euler distance varies with shape factor parameter k_0. (b) The experimental and GEMT model fitting results for the thermal conductivity of Al-xNi alloys (x = 6~25 wt.%).

accurate of the simulation results. The Euler distance fitting results of k_0 are shown in Fig. 14(a). For the shape factor k_0 = 120, the Euler distance is minimum. Therefore, k_0 is chosen to be 120 in this study. Then the predicted thermal conductivity of Al-xNi alloys by GEMT model can be obtained by Eq. (5). The experimental and GEMT model fitting results for the thermal conductivity of Al-xNi alloys are shown in Fig. 14(b), with the simulated value in line with the experiments.

5. Conclusions

The microstructure, thermal conductivity, electrical conductivity, and thermal expansion properties of Al-xNi alloys were investigated. Through the combination of experiments, first-principles calculations and theoretical models, the relationship between microstructure and thermal-physical properties was systematically studied. The main conclusions are:

(1) The microstructure in hypereutectic Al-*x*Ni alloys includes primary Al_3Ni and (α-Al + Al_3Ni) structures. With the Ni content increasing from 6 wt.% to 25 wt.%, the morphology of primary Al_3Ni does not change but the size increases significantly.
(2) With the increases of Ni content, CTEs and TCs show a decreasing tendency. The TC reduces from 202.8 W/(m·K) to 103.9 W/(m·K) as the Ni content increases from 6 wt.% to 25 wt.%, the CTEs decrease from 20.2 × 10^{-6}/K to 15.4 × 10^{-6}/K at the same time, showing improved expansion properties.
(3) The structure and thermodynamic properties of Al_3Ni were studied. At 100 °C, the CTE of Al_3Ni is 13.82 × 10^{-6}/K, showing excellent thermal expansion properties compared to pure Al.
(4) Based on the experimental and theoretical results, the relationship between microstructure and thermal-physical properties was quantified. The predicted CTE results by the revised Turner model are in good agreement with the experimental results. Besides, the general Effective Medium Theory model can provide a relatively accurate prediction for the TC of Al-*x*Ni alloys.

Declaration of competing interest

The authors declare that they have no known competing financial interests or personal relationships that could have appeared to influence the work reported in this paper.

Acknowledgement

This work was supported by the National Natural Science Foundation of China (No. 52174363). Computing resources from national supercomputer center in Guangzhou are gratefully acknowledged.

REFERENCES

[1] Barkov RY, Mikhaylovskaya AV, Yakovtseva OA, Loginova IS, Prosviryakov AS, Pozdniakov A. Effects of thermomechanical treatment on the microstructure, precipitation strengthening, internal friction, and thermal stability of Al–Er-Yb-Sc alloys with good electrical conductivity. J Alloys Compd 2021;855:157367.
[2] Wang M, Hu K, Liu G, Liu X. Synchronous improvement of electrical and mechanical performance of A356 alloy reinforced by boron coupling nano-AlNp. J Alloys Compd 2020;814:152217.
[3] Stadler F, Antrekowitsch H, Fragner W, Kaufmann H, Pinatel ER, Uggowitzer PJ. The effect of main alloying elements on the physical properties of Al–Si foundry alloys. Mater Sci Eng, A 2013;560:481–91.
[4] Hsieh CL, Tuan WH. Thermal expansion behavior of a model ceramic–metal composite. Mater Sci Eng, A 2007;460–461:453–8.
[5] Çadırlı E, Kaya H, Büyük U, Şahin M, Üstün E, Gündüz M. Investigation of the thermo-electrical properties of A707 alloys. Thermochim Acta 2019;673:177–84.
[6] Suwanpreecha C, Pandee P, Patakham U, Limmaneevichitr C. New generation of eutectic Al-Ni casting alloys for elevated temperature services. Mater Sci Eng, A 2018;709:46–54.
[7] Deng J, Chen C, Liu X, Li Y, Zhou K, Guo S. A high-strength heat-resistant Al–5.7Ni eutectic alloy with spherical Al_3Ni nano-particles by selective laser melting. Scripta Mater 2021;203:114034.
[8] Kakitani R, Reyes RV, Garcia A, Spinelli JE, Cheung N. Relationship between spacing of eutectic colonies and tensile properties of transient directionally solidified Al-Ni eutectic alloy. J Alloys Compd 2018;733:59–68.
[9] Fan Y, Makhlouf MM. The Al-Al_3Ni eutectic reaction: crystallography and mechanism of formation. Metall Mater Trans 2015;46:3808–12.
[10] Peng P, Zhang A, Yue J. Competitive growth of leading phase and tensile properties of directionally solidified eutectic Al–Ni alloy. Mater Sci Eng, A 2020;773:138887.
[11] Pandey P, Makineni SK, Gault B, Chattopadhyay K. On the origin of a remarkable increase in the strength and stability of an Al rich Al-Ni eutectic alloy by Zr addition. Acta Mater 2019;170:205–17.
[12] Wang K, Hu S, Zhong Y, Jin S, Zhou Z, Wang Z, et al. Effects of trace ytterbium addition on microstructure, mechanical and thermal properties of hypoeutectic Al–5Ni alloy. J Rare Earths 2022;40:1305–15.
[13] Hale DK. The physical properties of composite materials. J Mater Sci 1976;11:2105–41.
[14] Kerner EH. The elastic and thermo-elastic properties of composite media. Proc Phys Soc Sec. B 1956;69:808–13.
[15] Schapery RA. Thermal expansion coefficients of composite materials based on energy principles. J Compos Mater 1968;2:380–404.
[16] Turner PS. Thermal-expansion stresses in reinforced plastics. J Compos Mater 1946;37:239.
[17] Liu X, Zhou X, Mo L, Jiang M, Du J. Microstructural evolution and thermophysical properties of hypereutectic Al-22Si-xNi alloys prepared by sub-rapid solidification. J Mater Res Technol 2022;21:905–15.
[18] Su C, Li D, Luo AA, Ying T, Zeng X. Effect of solute atoms and second phases on the thermal conductivity of Mg-RE alloys: a quantitative study. J Alloys Compd 2018;747:431–7.
[19] Pan H, Pan F, Yang R, Peng J, Zhao C, She J, et al. Thermal and electrical conductivity of binary magnesium alloys. J Mater Sci 2014;49:3107–24.
[20] Chen JK, Hung HY, Wang CF, Tang NK. Thermal and electrical conductivity in Al–Si/Cu/Fe/Mg binary and ternary Al alloys. J Mater Sci 2015;50:5630–9.
[21] Aksöz S, Ocak Y, Maraşlı N, Çadirli E, Kaya H, Böyük U. Dependency of the thermal and electrical conductivity on the temperature and composition of Cu in the Al based Al–Cu alloys. Exp Therm Fluid Sci 2010;34:1507–16.
[22] Huang Y, Zhou X, Du J. Microstructure, thermal conductivity and mechanical properties of the Mg–Zn–Sb ternary alloys. Met Mater Int 2020;27:4477–86.
[23] Hamilton RL, Crosser OK. Thermal conductivity of heterogeneous two-component systems. Industrial 1962;1:182–7.
[24] Vaney JB, Piarristeguy A, Ohorodniichuck V, Ferry O, Pradel A, Alleno E, et al. Effective medium theory based modeling of the thermoelectric properties of composites: comparison between predictions and experiments in the glass–crystal composite system Si10As15Te75–Bi0.4Sb1.6Te3. J Mater Chem C 2015;3:11090–8.
[25] Rameshkumar S, Jaiganesh G, Jayalakshmi V. Structural, phonon, elastic, thermodynamic and electronic properties of Mg–X (X = La, Nd, Sm) intermetallics: the first principles study. J Magnesium Alloys 2019;7:166–85.

[26] Tong Z, Bao H. Decompose the electron and phonon thermal transport of intermetallic compounds NiAl and Ni_3Al by first-principles calculations. Int J Heat Mass Tran 2018;117:972–7.
[27] Qin G, Hu M. Accelerating evaluation of converged lattice thermal conductivity. npj Comput Mater 2018;4:1–6.
[28] Sun L, Gao Y, Xiao B, Li Y, Wang G. Anisotropic elastic and thermal properties of titanium borides by first-principles calculations. J Alloys Compd 2013;579:457–67.
[29] Varillas J, Očenášek J, Torner J, Alcalá J. Understanding imprint formation, plastic instabilities and hardness evolutions in FCC, BCC and HCP metal surfaces. Acta Mater 2021;217:117122.
[30] Shi D, Wen B, Melnik R, Yao S, Li T. First-principles studies of Al–Ni intermetallic compounds. J Solid State Chem 2009;182:2664–9.
[31] Harsha Gunda NS, Michi RA, Chisholm MF, Shyam A, Shin D. First-principles study of Al/Al_3Ni interfaces. Comput Mater Sci 2023;217:111896.
[32] Alias FIH, Ridzwan MH, Yaakob MK, Loy CW, Mohamed Z. Structural, electronic and optical studies of Sr_2NiTeO_6 double perovskite by first-principle DFT–LDA + U calculation. J Mater Res Technol 2022;18:1623–30.
[33] Wu E, Qiu N, Luo K, Chen X, Shi D, Bu M, et al. The studies of electronic structure, mechanical properties and ideal fracture behavior of $U_3Si_{1.75}Al_{0.25}$: first-principle investigations. J Mater Res Technol 2021;15:1356–69.
[34] Rudajevová A. Thermal diffusivity of plasma sprayed alumina coatings. Mater Res Bull 1991;26:1363–9.
[35] Leitner J, Voňka P, Sedmidubský D, Svoboda P. Application of Neumann–Kopp rule for the estimation of heat capacity of mixed oxides. Thermochim Acta 2010;497:7–13.
[36] Kresse GG, Furthmüller JJ. Efficient iterative schemes for ab initio total-energy calculations using a plane-wave basis set. Phys Rev B 1996;54:11169.
[37] Perdew JP, Burke K, Ernzerhof M. Generalized gradient approximation made simple. Phys Rev Lett 1996;77:3865–8.
[38] Gonze X. Adiabatic density-functional perturbation theory. Phys Rev 1995;52:1096–114.
[39] Blanco MA, Francisco E, Luaña V. GIBBS: isothermal-isobaric thermodynamics of solids from energy curves using a quasi-harmonic Debye model. Comput Phys Commun 2004;158:57–72.
[40] Togo A, Tanaka I. First principles phonon calculations in materials science. Scripta Mater 2015;108:1–5.
[41] Yanxunoto A, Tsubakino H. Al_9Ni_2 precipitates formed in an Al-Ni dilute alloy. Scripta Mater 1997;37:1721–5.
[42] Plata JJ, Usanmaz D, Nath P. Predicting the lattice thermal conductivity of solids by solving the Boltzmann transport equation: AFLOW-AAPL an automated, accurate and efficient framework. 2016. p. 1–11.
[43] Curtarolo S, Setyawan W, Hart GLW, Jahnatek M, Chepulskii RV, Taylor RH, et al. AFLOW: an automatic framework for high-throughput materials discovery. Comput Mater Sci 2012;58:218–26.
[44] Wei Z, Ma P, Wang H, Zou C, Scudino S, Song K, et al. The thermal expansion behaviour of SiCp/Al–20Si composites solidified under high pressures. 1980-2015 Mater Des 2015;65:387–94.
[45] Rocha RPA, Cruz MAE. Computation of the effective conductivity of unidirectional fibrous composites with. AN interfacial thermal resistance 2001;39:179–203.
[46] Carotenuto G, Buonanno A. The effective thermal conductivity of packed beds of spheres for a finite contact area. Numer Heat Tran, Part A: Applications 2000;37:343–57.
[47] Wang J, Carson JK, North MF, Cleland DJ. A new approach to modelling the effective thermal conductivity of heterogeneous materials. Int J Heat Mass Tran 2006;49:3075–83.